**Solid Freeform Fabrication 2024: Proceedings of the 35th Annual International Solid Freeform Fabrication Symposium – An Additive Manufacturing Conference**
**Reviewed Paper**

# USE OF CORED WIRE IN THE OPTIMISATION OF NEW ALLOYS FOR LASER POWDER BED FUSION WITH TAILORED MECHANICAL AND CORROSION PROPERTIES

E. Palmer[1], S. Mehraban[1], D. Butcher[1], M. Ritchie[1], T. Abdullah[1], L. Neto[2], M. Cordero[2], G. Stratford[3], N. P. Lavery[1]

[1]MACH1 Laboratories, Faculty of Science and Engineering, Swansea University, UK, SA1 8EN

[2]Welding Alloys Group, UK, CB21 6DD

[3]LSN Diffusion, UK, SA18 3GY

## Abstract

The utilisation of cored wire is of significant interest in both wire and powder-based Additive Manufacturing (AM) processes, providing the ability to undertake in-situ alloying additions and rapidly assess the influence of composition on properties.

This study compares the processing of 316L by Laser Powder Bed Fusion (L-PBF) using powders produced by Gas Atomisation (GA) and cored-wire Ultrasonic Atomisation (UA). The cored-wire Ultrasonic Atomisation (UA) is a novel technique allowing in-situ compositional changes using balanced levels of alloying elements such as molybdenum within the core. The ongoing investigation has focussed on verifying composition (including Carbon, Oxygen and Nitrogen) through the entire process, comparing GA and UA powder morphology and sizes, as well as analysis of the as-built L-PBF material quality. The mechanical testing included tensile strength and density, while corrosion resistance was assessed through change in corrosion potential, linear polarisation resistance and pitting potential.

This research demonstrates the ability to optimise alloy compositions, facilitating the development of tailored 316L steels for AM with desired mechanical and corrosion properties. This work shows how cored-wire coupled with Ultrasonic Atomisation can be used to produce 316L for L-PBF with comparable densities, mechanical and corrosion properties to traditional Gas Atomised powder.

**Key Words:** Tailored Alloy Design, Laser Powder Bed Fusion, Powder Atomisation

## Introduction

Additive layer manufacturing (ALM) has seen increased uptake in the field of material science and engineering, offering flexibility in the design and production of complex geometries with customised materials. Due to its flexibility, ALM has attracted use among aerospace, automotive and medical among other sectors. Among the various techniques utilised within AM, both wire and powder-based processes have gained significant attention due to their versatility and

potential in rapid prototyping and alloy down selection addressing the growing demand for high-performance materials with tailored characteristics. In the field of ALM, laser powder bed fusion (L-PBF), alternately known as selective laser melting (SLM), has enabled the manufacture of small components by melting small layers of metal powder. This is performed using a high-powered laser and creating a three-dimensional part on a layer-by-layer basis. In addition, L-PBF provides the ability to create fully dense parts across a range of metal alloys.

One area of exploration which has evolved at a slower pace is alloy design of new alloys specifically tailored to ALM. This may seem counter intuitive as it has been known for over twenty years that the use of wrought or casting alloys (e.g. Ti-6Al-4V, INC738, AlSi12…) did not work as well when processed by ALM, [1], [2]. The higher cooling rates can lead to significant variations in micro-compositions, different microstructures, and phases which do not arise in the original alloy processing route.

The best-known example of ALM-focussed alloy development is the ScalmalloyRP® developed by EADS in the early 2000s. Based on a 5-XXX composition (Al-Mg-Sc-Zr), the aim was to get a high-strength, corrosion resistant and weldable alloy which would process better in ALM, particularly L-PBF, [3]. The addition of Sc improved strength and ductility through a combination of mechanisms, including precipitation hardening after annealing, grain refinement (Sc/Zr), as well as high solid solution hardening which benefited from the higher cooling rates [4]. Subsequent generations (ScanCromal®, ScanTital®, …), aimed at reducing the Sc because of cost/availability and to accommodate L-PBF processing problems such as the evaporation of Mg [5].

Much of the early development of SalmalloyRP relied upon theoretical and laboratory casts in which one element (e.g. Sc) is optimised over 3-4 levels, followed by a scale-up to atomisation using ball-milled or ribbon-cast feedstock, [6]. The need for powders of sufficient quantity and quality (composition, morphology and size distributions) to be processable by L-PBF is one of the main bottlenecks in adopting a broader compositional exploration. Pre-alloyed gas atomised powder is expensive for small quantities (<10kg) and can have a relatively long lead time. Even a coarse full factorial design of experiments with 2 or more elements over 3 levels becomes prohibitive, especially if larger batches are needed for mechanical property campaigns. Alternative efforts to use ball-milled powder or in-situ blended elemental powder, [7], [8], [9], are hampered by limitations in powder quality, contamination and achieving homogeneous chemistries when processed by L-PBF, which can be tricky depending on the composition.

More recently, CALPHAD has been used with machine learning coupled with assisted alloy selection and casting-based prototyping on the Al-Mg-Sc-Zr system can be found in [10]. The authors point out that even with assisted sampling, the limited experimental data makes extrapolation difficult to wider compositional ranges. Whilst machine learning (M/L) is a promising route it still needs to be coupled with faster prototyping representative of the higher cooling rates of L-PBF, and higher throughput characterisation of properties.

Two relatively new technologies promise to break this impasse in alloy design for L-PBF. The first is Ultrasonic Atomisation (UA), [11], [12], [13], which has the capability of making small batches of powder with the necessary quality for L-PBF. It is a flexible process that is able to atomise a wide range of metal alloys and maintain composition from feedstock to printed parts. The second technology is the use of cored wire, where the core is a balance of elemental additions

to achieve the desired compositions, [14]. However, as a new combined technology the full potential and limitations are as-yet unknown.

In the current work, the authors decided to commence exploration of in-situ alloying using cored wire and ultrasonic atomisation to tailor the properties of 316L powder for L-PBF. The choice of 316L stainless steel as a starting alloy is because it is widely recognised for its mechanical properties and corrosion resistance and has been extensively studied and compared to traditional processing, such as casting and forging routes. The processing chain is increasingly well understood with respect to laser parameters, [15], post-build heat treatments including annealing and hot-isostatic pressing, [16], powder characteristics and requirements in during L-PBF processing, [17], [18]. The levels of control on porosity and microstructures of L-PBF 316L, and their relative contributions to properties including tensile strength, fatigue, impact strength and corrosion, [17], [19], [20], are allowing standards to be set for rapidly evolving machines, taking L-PBF into the industrialisation phase.

The extensive prior work on 316L makes it a great starting point for testing the potential and limits of the new powder alloy production, testing compositional control at both the higher alloying levels (Cr, Ni) and lower alloying levels (Mn, Mo), as well as the control available on C and impurities Si, S, P, N, and O. To this extent, the current study set out to firstly compare the processability of UA powder as compared to GA powder, and secondly assess the use of a cored-wire feedstock to derive the UA powder. The comparison was to be done based on powder characterisation (chemistry, morphology and size distributions), the density, hardness and microstructures of the L-PBF builds and the mechanical properties (tensile) and corrosion properties (corrosion potential, linear polarisation and pitting potential) of the as-built material using both powders. These can all be put in the context of the extensive work on 316L as a common baseline, paving the way for tailored alloy development, which might involve minor alloying optimisation (e.g. by varying molybdenum). An important step will be that compositions from wire to powder to as-built material are traced and compared to the AISI 316L standard chemistry, including levels of impurities such as O and N.

## Experimental Materials and Methods

### Cored Wire Analysis

Cored wire was prepared by Welding Alloys Group for 316L with a composition given in Table 1, which can be seen to be within the AISI specification, apart from carbon which is slightly higher. The composition was measured at different locations along the wire, so the standard deviation represents the acceptable levels of local variation. Cored wire is produced via a sheath of stainless steel filled with a mixture of pure elemental powders made up to a normalised composition of the desired alloy. An SEM cross-section of the wire can be seen in Figure 1 (a). The EDS map allows the elemental additions in the core to be differentiated.

### Ultrasonic Atomisation

The cored wire was processed into powder using the ATO Lab+ from 3DLAB. This ultrasonic atomiser operates under Argon and makes use of a TIG torch to melt wire on to a 35 KHz sonotrode. Each batch of powder produced using this frequency was top cut to a mesh size of 63µm, giving 5kg of usable powder. A 52 KHz sonotrode available is also available in the ATO

Lab+, but was not used in this study, to have a broader and more comparable size fractions to the gas atomised powder. The increase in ultrasonic frequency increases liquid melt breakup on the sonotrode and produces finer powder sizes, [11].

## Gas Atomised Powder

A 316L gas atomised powder was provided by LSN diffusion for the baseline. The composition of this powder was measured by ICP and is given in Table 1. As can be seen, the composition of this powder passes all the elemental limits required by the AISI 316L standard.

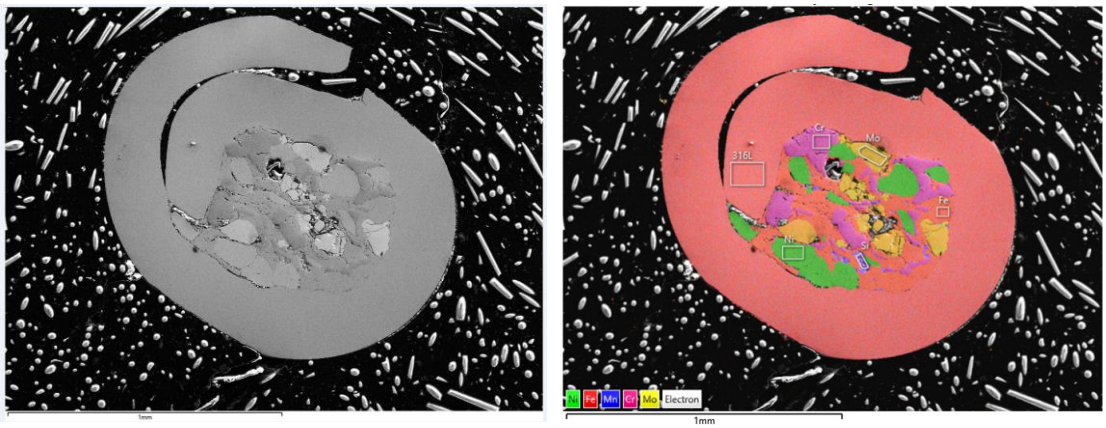


(a) (b)

**Figure 1 – (a) SEM image of a cross-section of the 316L cored wire (b) EDS mapping**

## Particulate Measurements

The powder size distribution measurements were performed on a Malvern Mastersizer 3000. The Mastersizer is a wet system in which the powders are suspended in deionised water. The Mastersizer uses laser diffraction to analyse particles ranging from 0.1 to 2500 µm. Ten measurements were performed for each powder sample to provide an average for each test.

## Tensile Testing

The tensile test bars were built based on a scaled ASTM-E8 sub-specimen, with a gauge length of 20mm and a thickness of 3 mm. The bars on the plate are shown in Figure 8 (a) for the GA-316L powder and (b) for the AU-316L powder, and these were printed with a skin and sandblasted after taking off the plate. The tensile testing was done on a Tinius-Olsen 25kN universal testing machine with a DIC video extensometer. Strain rates were based on ASTM/BSI standard of 0.015 mm/mm/min and accelerated after yield to 0.4 mm/mm/min.

## Results and Discussion

### Chemical Compositions (Wire, Powder, AM)

The AISI standard composition for 316L is given in Table 1. Also given are measured compositions using ICP for main elements, ELTRA for O and N, and LECO for C and S. As can be seen from the measurements of the gas atomised powder and the wire feedstock for the UA powder, there are some differences between them, but both are mostly within the AISI specification. Comparing the cored wire and GA powder, the Ni is about 2.4% higher, the Mo is about 0.7% higher, and Mn, Cr and Si are about 0.1% higher. The cored wire was sampled at various points along the wire, so the levels of standard deviation are also indicative of local variance, but do not take the main elements outside the AISI specifications. Importantly, there are no major losses during ultrasonic atomisation of the cored wire or during the L-PBF processing.

The cored wire levels of C are slightly higher than the AISI specification, but after atomisation the overall levels of C and N of the powders are within the AISI specification, and certainly the C levels are not significantly different in the final L-PBF material.

The GA powder is slightly higher in N than the specification, which may be on purpose, but much higher than both the cored-wire and UA powder are significantly lower. This high N content in the GA powder leads to a higher N in the L-PBF material than the UA powder. Nitrogen in 316L is known to be important, leading to higher hardness, yield and tensile strength, [21].

Although there is no AISI limit for 316L oxygen levels, they are important as oxygen also influences mechanical and corrosion properties, [22]. While higher levels are expected in atomised powders, the GA powder is typical from gas atomisation at 500 ppm at these size fractions. The oxygen levels in the solid cored wire were similar to that of the GA powder at 550 ppm but seem to drop in the powder after ultrasonic atomisation to an average of 510 ppm. This was found to vary between size fractions and could be as high as 600ppm in the sub 45µm size fraction. This is thought to be something which can be reduced in both the cored-wire and ultrasonic atomisation processing but changing parameters and possibly using the 50 kHz sonotrode. The levels of oxygen in the final solid L-PBF materials made from the UA powder averaged around 490 ppm, displaying a small decrease.

| | | GA-316L | | UA-316L | | |
|---|---|---|---|---|---|---|
| **Elem. (wt.%)** | **AISI 316L** | **Powder** | **L-PBF** | **Wire** | **Powder** | **L-PBF** |
| **Fe** | Bal. | 67.68 | 67.51 | 64.4±0.61 | 64.9 | 64.4 |
| **Cr** | 16-18 | 16.7 | 16.78 | 16.8±0.65 | 17.21 | 18 |
| **Cu** | - | 0 | 0.02 | 0.09±0.006 | 0.04 | 0.05 |
| **Mn** | < 2 | 1.32 | 1.3 | 1.4±0.05 | 0.58 | 0.42 |
| **Mo** | 2-3 | 2.3 | 2.36 | 2.9±0.16 | 2.71 | 2.88 |
| **Ni** | 10-14 | 11 | 11.28 | 13.4±0.14 | 13.41 | 13.31 |
| **P** | < 0.045 | 0.01 | 0.007 | 0.015±0.001 | 0.016 | 0.019 |
| **Si** | < 0.75 | 0.5 | 0.52 | 0.58±0.015 | 0.67 | 0.59 |
| **C** | < 0.03 | 0.0136±0.0008 | 0.016±0.009 | **0.037±0.006** | 0.015±0.0004 | 0.015±0.0005 |
| **S** | < 0.03 | 0.0063±0.0007 | 0.00585±0.00021 | 0.009±0.0006 | 0.008±0.0003 | 0.00767±0.0005 |
| **O** | - | 0.05 | 0.05 | 0.055±0.00013 | 0.051±0.0024 | 0.049±0.00021 |
| **N** | < 0.1 | **0.12** | 0.1 | 0.029±0.0010 | 0.019± 0.00048 | 0.017±0.00011 |

**Table 1 – Composition as measured by ICP (Fe, Cr, Cu, Mn, Mo, Ni, P, Si), LECO (C, S) and ELTRA (O, N).**

## Powder Characterisation (Particle Size Distributions and Powder Morphology)

SEM images of the powders are shown in Figure 2. The as-atomised powder size distributions as determined using a Malvern Mastersizer 3000 are given in Table 2. The normal distributions for the powders are shown in Figure 3.

In terms of the powder morphology the SEM images in Figure 2 show that the ultrasonic atomised (UA) powder is highly spherical, compared to the gas atomised (GA) powder, which is generally spherical, but which has a greater number of elongated particles and satellites. Satellites in gas atomisation are caused by smaller particles colliding with larger particles which have not yet fully solidified inside of the atomisation chamber. Due to the aggressive liquid droplet formation caused by the high-pressure gas stream, GA powder may include more irregular morphologies. The UA particles have a smooth surface but do also have small satellites, which are thought to be from irregular splatter during the ultrasonic droplet shedding.

There are also distinct differences in the sizes of the powder particles which although also generally spherical, the GA can be seen to have a wider distribution of small to large particles, whilst the UA particles are more mono-dispersed. This is reflected in the normal distributions in Figure 3, where the GA distribution in blue is centred around the D50 median of 44µm and has a higher volume of smaller particles. The sieved AU powder shows a sharp peak around a median of 49µm, and the change in distribution after sieving is clear, shifting the median from 55.3µm to the left, and giving a much higher volume around the D50.

The size fractions in each of the D10, D50, and D90 for the UA and GA powders are given in Table 2. Neither the UA and GA powder would be considered ideal for L-PBF, which usually use slightly finer powders in the 15-45 µm with more typical values of the D10, D50 and D90 being 20µm, 30µm and 45µm, respectively. However, the slightly oversized fractions make a direct comparison fairer.

The tap densities were measured as 56.93±0.87% (4.55 g/cm$^3$) for the GA powder, and 58.15±0.87% (4.65 g/cm$^3$) for the UA-316L powder, which are typical for 316L powder, [23]. The

hall-flow measurements for the GA powder averaged 16.49±0.02 s/50g, and for the UA powder 13.08±0.02 s/50g, which are lower than the more typical 17s, showing that the powder flows well, which might be expected from the high levels of sphericity.

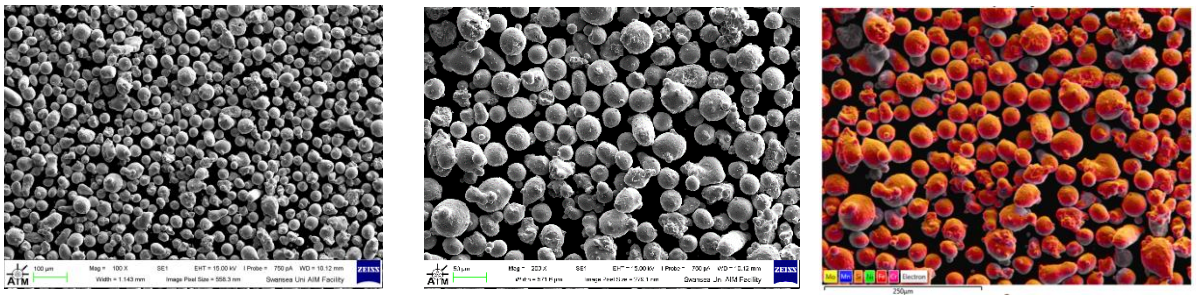

(a) GA316L (100X) (b) GA316L (200X) (c) GA316L (200X, EDS)

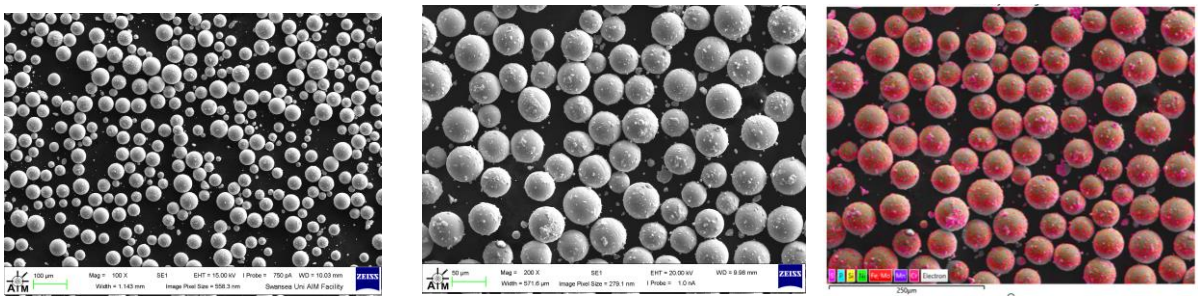

(d) UA-316L (100X) (e) UA-316L (200X) (f) UA-316L (200X, EDS)

**Figure 2 – SEM/EDS Images of the powders**

| | D10 (µm) | D50 (µm) | D90 (µm) | Note |
|---|---|---|---|---|
| **GA-316L** | 30.0 | 44.8 | 69.5 | Gas Atomised Powder |
| **UA-316L** | 37.6 (37.6) | 49 (55.3) | 63.7 (82.5) | Ultrasonic Atomised Powder from wire. Values in brackets are prior to sieving. |

**Table 2 – Malvern Mastersizer measurements volume-based particle size distributions for atomised powders**

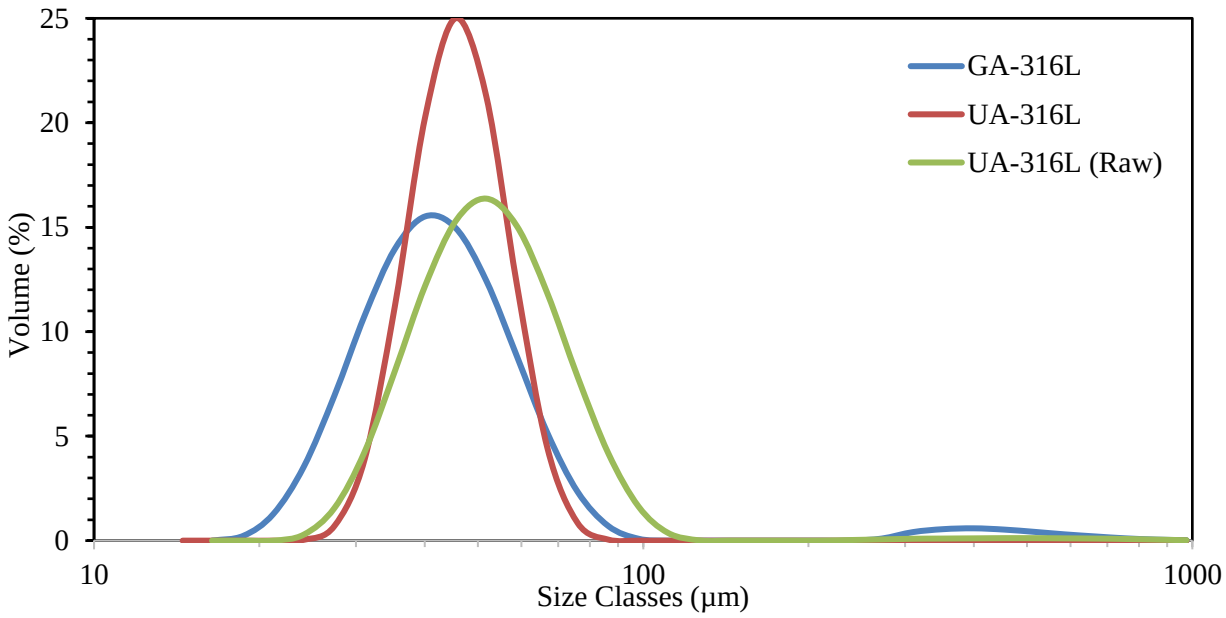


**Figure 3 – Particle size distributions as measured by the Malvern Mastersizer**

## L-PBF Production of Samples

The L-PBF builds for this work was done on a Renishaw AM400, in the Reduced Build Volume (RBV) which uses a smaller 80mmX80mm build plate, and allows build heights of up to 55 mm. This differs from the full build plate (250mmX250mmX285mm) in the size of the build volume, requiring much less powder for each build. However, an additional difference is that the RBV does not have a heated build plate. Each powder underwent 2 builds:

**Builds B1 -** The first was an optimisation step using a Box-Behnken Design (BBD) of experiments in which 3 machine parameters were varied (Power, Point Distance, Exposure Time) with hatch spacing kept constant at 110 µm. Response surface methodologies (RSM) utilise quadratic terms, allowing them to model curvature in the response, unlike factorial designs, which use linear terms. Another advantage of RSM is the reduced number of experimental runs required compared to full factorial designs. There are two types of response surface designs Centralised Composite Designs (CCD) and BBD. Due to the size limitations of the RBV a BBD was selected as these require fewer experimental runs, 13 as opposed to 18 with a single centre point; this is due to the exclusion of the experimental runs where all factors are at their extremes and the axial points utilised in a CCD. Despite this reduction in experimental runs, BBD are still able to effectively estimate the first and second order coefficients. The parameter sets were based on the parameters typically used for 316L and are shown in Table 3. Photos of the optimisation builds for the gas atomised powder (GA-316L) and the ultrasonic atomised powder UA316L-are shown in Figure 4. Relative density was measured using optical microscopy (Zeis Observer Z1 at magnification 50X, giving 25 stitched images), as shown for various parameter sets in Figure 5, where the black areas are mostly pores. Image analysis gave relative densities of between 99.61% and 99.91% for the GA powder, and between 99.25% and 99.79% for the UA powder, as shown in Figure 6 (a). The worst parameter set for both powders was A12, with the lowest relative density which is not surprising as this was also the set with the smallest Volumetric Energy Density. For this set, there

is evidence in the builds from both powders of irregular pores along laser tracks, suggesting a lack of fusion, which can be seen looking closely at Figure 5 (a) and (d). However, set A7 with the highest volumetric energy density also resulted in the lowest porosity in the GA powder, and second lowest in the UA powder. The hardness of the GA-316L samples (A7) was 233HV±11 in the XZ direction and 242HV±6 in the XY direction. The measured hardness of the UA-316L samples (A7) was 194HV±7 in the XZ direction and 188HV±7 in the XY direction.

Microstructures in the build direction for the as-built samples at the optimal settings (A7) for GA-316L are compared to UA316Lpowders in Figure 7. The melt pools can be clearly seen, and they appear to be more lenticular in the case of the UA powder, whereas the GA powder shows a higher aspect ratio of the melt pool with deeper penetration. This could possibly be due to the slightly larger powder particles requiring more energy to melt. Higher magnification of the melt pools using SEM in Figure 7 (c) and (d) show a number of features common to 316L made by L-PBF, [24], [25], fusion boundaries an a sub grain cellular structures that form due to the high cooling rates, with columnar grain structures perpendicular to the build plate.

**Builds B2 –** Based on the fact that both powders had relatively low porosity and set A7 was the best or second best for both powders, it was decided that this set would be used for Builds B2 for the tensile and corrosion samples. Photos of these builds with both powders are shown in Figure 8 (a) GA and (b) UA.

| Parameter Set | Power (W) | Exposure time (µs) | Point distance (µm) | VED (J/mm$^3$) |
|---|---|---|---|---|
| **A1** | 180 | 80 | 55 | 47.60 |
| **A2** | 200 | 70 | 65 | 39.16 |
| **A3** | 220 | 90 | 60 | 60.00 |
| **A4** | 200 | 90 | 55 | 59.50 |
| **A5** | 180 | 80 | 65 | 40.28 |
| **A6** | 220 | 70 | 60 | 46.67 |
| **A7** | 220 | 80 | 55 | 58.18 |
| **A8** | 200 | 70 | 55 | 46.28 |
| **A9** | 220 | 80 | 65 | 49.23 |
| **A10** | 200 | 90 | 65 | 50.35 |
| **A11** | 200 | 80 | 60 | 48.48 |
| **A12** | 180 | 70 | 60 | 38.18 |
| **A13** | 180 | 90 | 60 | 49.09 |

**Table 3 – Design of experiments used for all powders (Builds 1). Hatch spacing was kept constant at 110 µm.**


(a) (b)

**Figure 4 – Optimisation builds B1 for (a) Gas Atomised powder (GA-316L) and (b) Ultrasonic Atomisation powder (UA-316L)**

| **Cubes from GA-316L powder** | | |
|---|---|---|
| 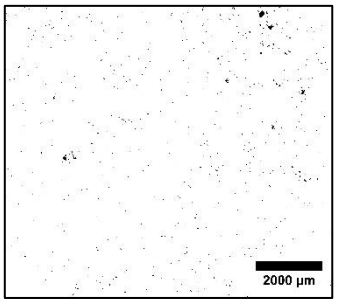 | 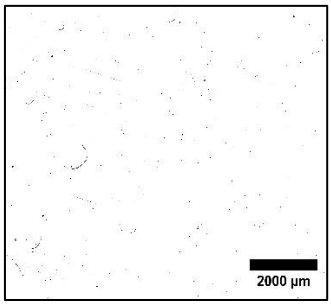 | 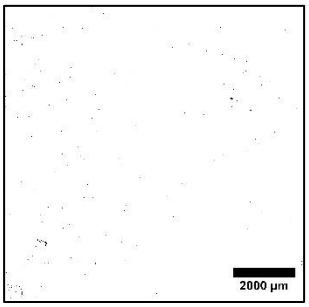 |
| (a) A12 (99.61%) | (b) A11 (99.77%) | (c) A7 (99.91%) |
| **Cubes from UA316L-3Mo** | | |
| 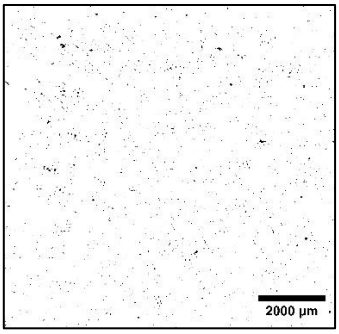 | 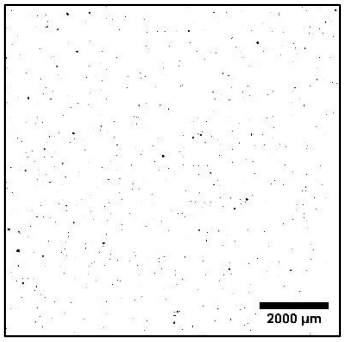 | 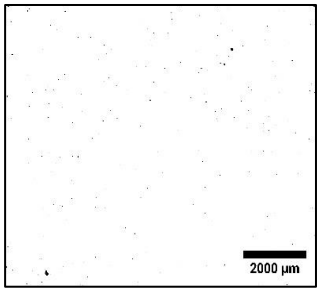 |
| (d) A12 (99.25%) | (e) A13 (99.64%) | (f) A9 (99.79%) |

**Figure 5 – Rendered optical microscopy showing porosity in X-Y direction for GA (a-c) and UA (d-f) powders, together with the parameter set giving the lowest, medium and highest density.**

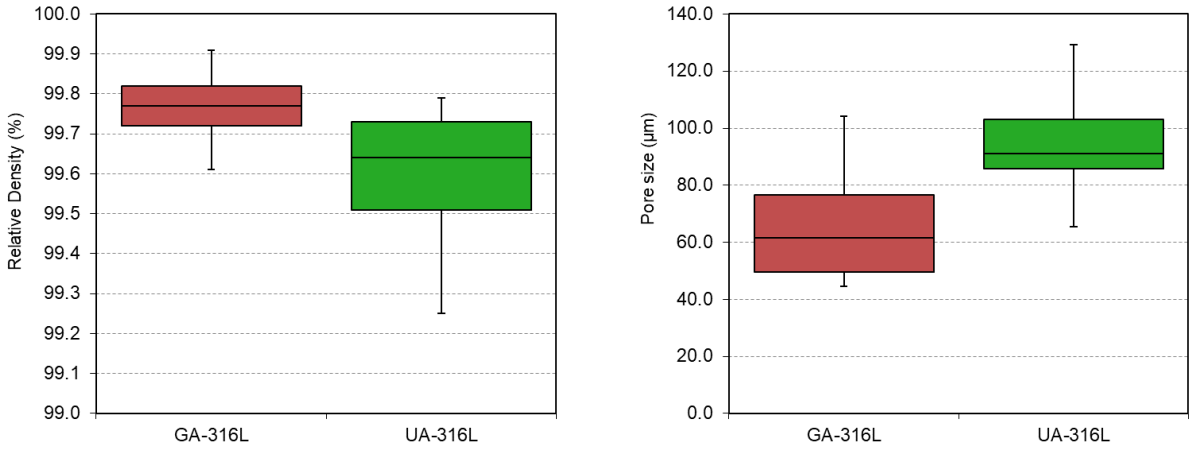


**Figure 6 – (a) Relative density for both powders as measured by image analysis and (b) average pore size, as measured from optical microscopy image analysis**

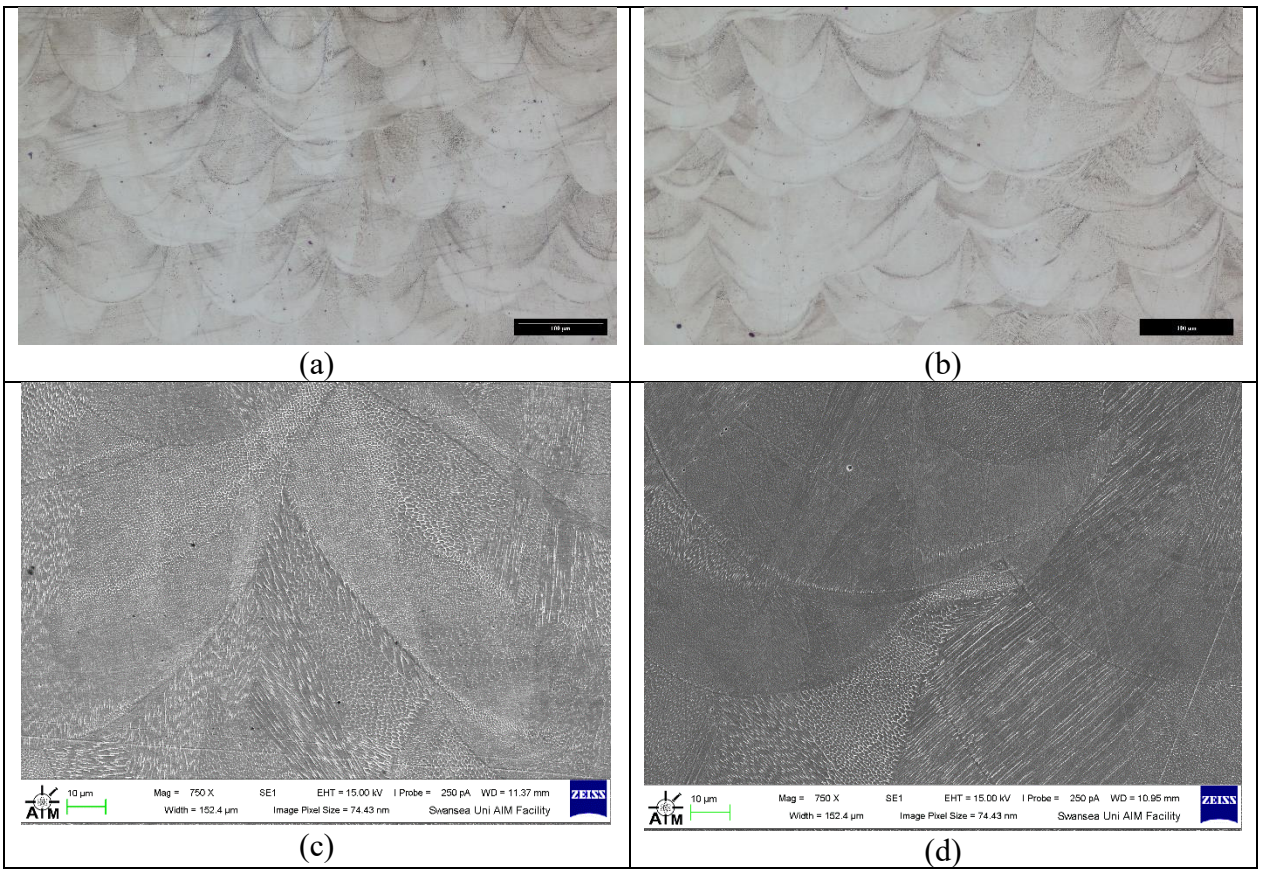


**Figure 7 – Optical and SEM micrographs of L-PBF cubes (set A7) showing melt pools for builds with powder from (a,c) Gas Atomisation and (b,d) Ultrasonic Atomisation**

| Powder | Power (W) | Exposure time (µs) | Point distance (µm) | Hatch Spacing (µm) | Volumetric Energy Density (J/mm$^3$) | Measured density or porosity (%) | Average Pore Size (µm) |
|---|---|---|---|---|---|---|---|
| **GA-316L (A7)** | 220 | 80 | 55 | 110 | 58.18 | 99.91 | 44 |
| **UA-316L (A7)** | 220 | 80 | 55 | 110 | 58.18 | 99.74 | 103 |

**Table 4 – Parameters in set A7 were chosen as optimal for subsequent builds with GA and UA atomised powders**

## Tensile Testing Results

As can be seen from the stress-strain curves in Figure 9, and summarised in Figure 10, the Gas Atomised powder has a 60 MPa higher tensile strength than the Ultrasonic Atomised powder. The actual UTS values of 507 MPa (UA) and 567 MPa (GA) are slightly lower than would be expected for an optimised L-PBF 316L steel, which is typically about 600 MPa, [16], [20], [24], but the average elongation to failure of both powders at 45% is higher than the expected 40% outlined in the standard ASTM A240 specification. It is possible that the dimensions of the tensile specimen used (as it is slightly smaller than the ASTM standards) may have resulted in higher elongations and lower strengths.

However, the difference between the two powders could come from a combination of causes, including higher nitrogen in the GA powder, higher density of the fused material from the GA powder, and be related to the slightly smaller particle sizes in the GA powder. A quick check of the relative compositions using the relationship between UTS and composition of austenitic steels, [26], indeed shows that the most likely increase in strength of 50 MPa is driven by the higher N content.


(a) (b) (c)

**Figure 8 – Tensile builds B2 for (a) Gas Atomised powder (GA-316L), (b) Ultrasonic Atomisation powder (UA-316L) and (c) Dimensions of the 3mm thick tensile test bars.**

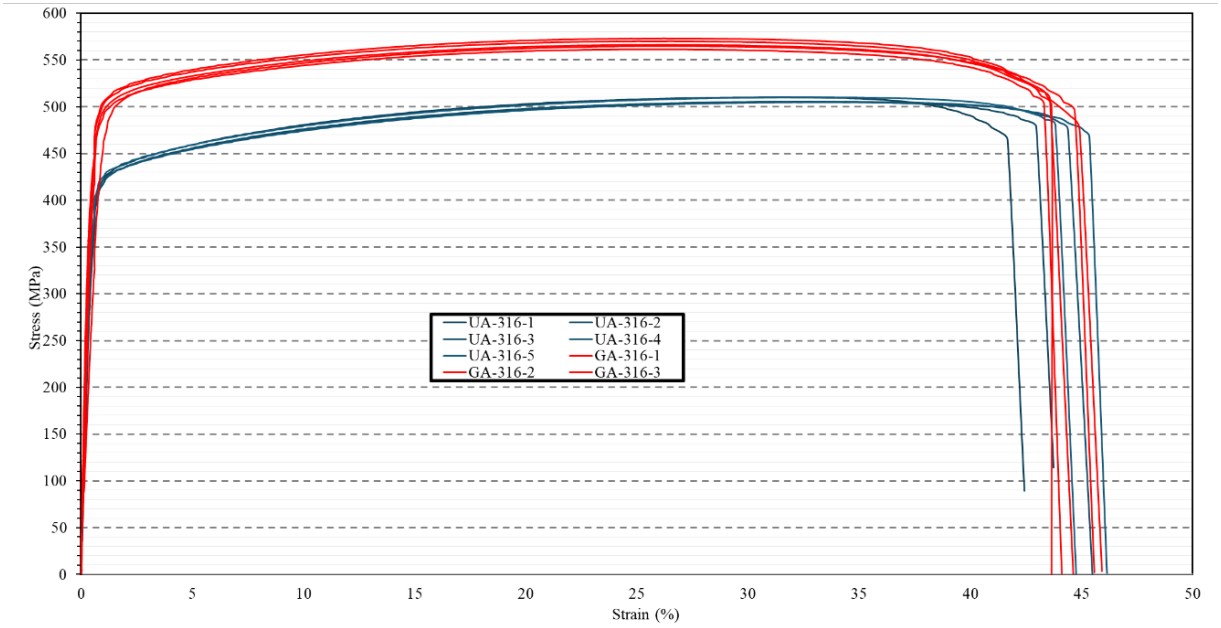


**Figure 9 – Stress-strain curves from the tensile testing, showing all samples from Ultrasonic Atomised powder (blue) and Gas Atomised powder (red).**

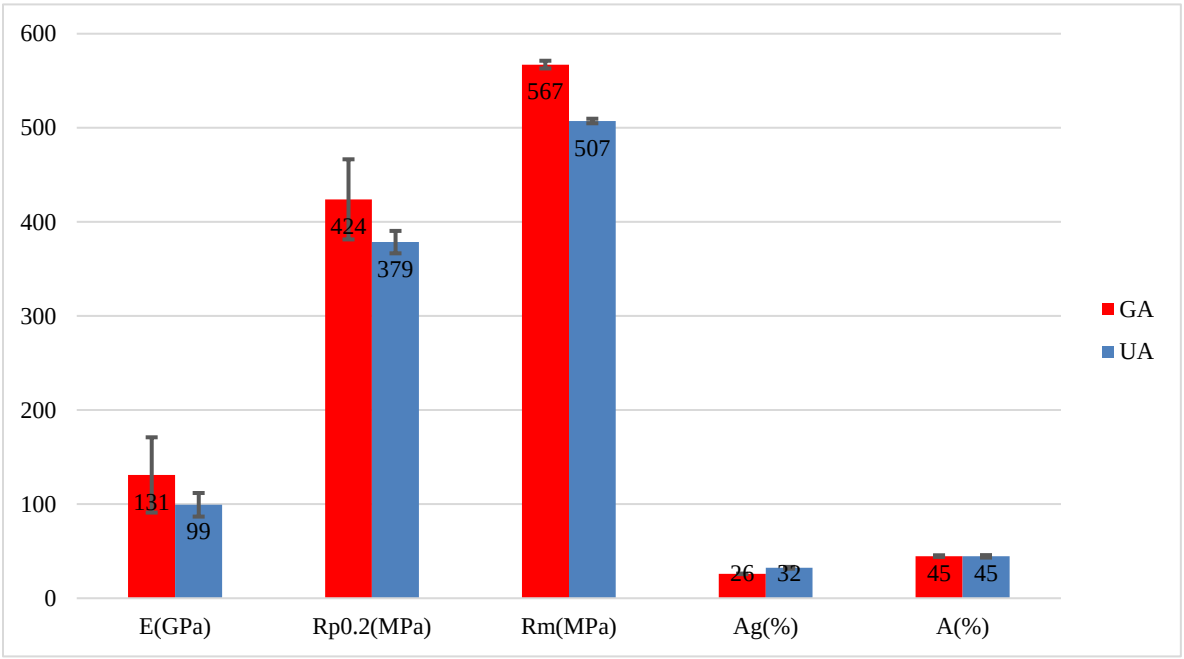


**Figure 10 – Tensile properties for L-PBF samples derived from Ultrasonic Atomised powder (blue) and Gas Atomised powder (red).**

## Cyclic Polarisation Corrosion Testing

To investigate the corrosion behaviour of the two atomisation methods once printed, the Potentiodynamic polarization test was used. The $E_{pit}$ is identified by observing the potential at which there is a continuous rise in the anodic current density, indicating ongoing localized dissolution of the alloys due to the breakdown of the protective oxide or passive film on the surface [27].

A GAMRY 1010 potentiostat was used in a three-electrode setup with the sample as the working electrode for cyclic potentiodynamic polarization [28]. The reference electrode used was a saturated calomel electrode, and a platinum-plated electrode served as the counter electrode. The reference electrode was placed close to the working electrode, the counter electrode was positioned 10cm away from the SCE. The conducting solution was deaerated 3.5%wt NaCl. Potentiodynamic scans were initiated 200 mV below the open circuit potential and proceeded in the positive direction at a rate of 0.166 mV/s. The scan direction was reversed once a potential voltage 1.5V above OCP was achieved and the test ended on return to the initial starting potential. These parameters were selected to facilitate pitting and re-passivation of the material and capture the complete polarisation loop. Experiments were performed in accordance with ASTM standards G 61–86 [29] and G 59–97 [30].

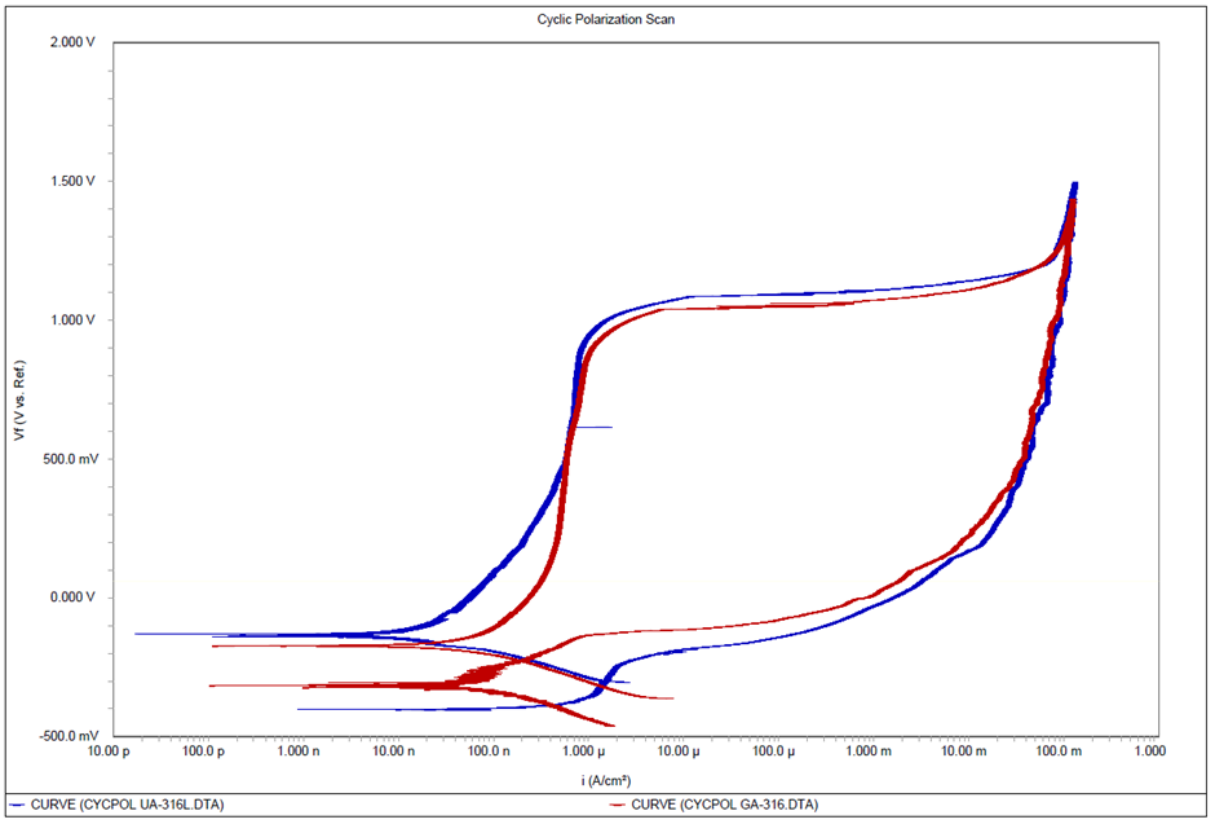


**Figure 11 – Cyclic polarisation plots for AM printed UA-316L and GA-316L, with extracted values for Ecorr, Epit, Icorr and IPass displayed in table 1**

| Sample | $E_{corr}$ (V vs SCE) | $E_{pit}$ (V) | $I_{corr}$ (A/cm^2) | $I_{pass}$ (A/cm^2) |
|---|---|---|---|---|
| GA- 316L | -0.173 | 0.899 | 8.39E-08 | 1.08E-06 |
| UA-316L | -0.133 | 0.919 | 3.47E-08 | 1.02E-06 |

**Table 5 –Summary of corrosion data for each powder atomisation method**

The obtained parameters shown in Table 5 include the corrosion potential ($E_{corr}$), corrosion-current density ($I_{corr}$), pitting potential ($E_{pit}$) and passive current density ($I_{pass}$), as shown in Figure 11, which is a typical polarization curve in a 3.5 wt % NaCl solution. The values for $E_{pit}$ are comparable to previously measured values for AM 316L material [31].

A comparison of UA-316L and GA-316L powder produced AM samples indicates that the $E_{corr}$ and $E_{pit}$ and are comparable between both methods of atomisation. Samples display negative hysteresis indicating that localised corrosion has initiated and will not re-passivate due to pitting to arrest the corrosion reaction. This is due to the large potential applied to the samples to allow for the full polarisation loop to be captured. A maximum applied potential of approx. 1.2mV vs SCE could be used if samples are retested to capture re-passivation kinetics in finer detail.

It has been shown that corrosion resistance in L-PBF samples is decreased due to LOF (lack of fusion) pores due to their susceptibility to act as pit formation sites [32]. Sample UA-316L shows a larger hysteresis indicating a lower likelihood that re-passivation could take place, this may be due to the higher level of porosity in the sample when combined with a larger average surface pore size may drive corrosion reactions further than for GA-316L.

## Conclusions

The overall goal of the current work is to eventually have a physical alloy development process specifically for new alloys for laser powder bed fusion which is faster than the conventional route. To get to this stage, two fundamental steps need to be assessed across a wide spectrum of parameters which are required for an optimal L-PBF process, namely using a cored-wire for in-situ alloy feedstock and secondly the use of ultrasonic atomisation.

The linking of these two steps is thought to be a first by the authors, and work has shown that a 316L composition can be obtained from the cored wire and ultrasonic atomisation approach, which is within the AISI specification, and this is ultimately tuneable and capable of extension to other alloys. It has shown where some of the potential difficulties are with respect to for example nitrogen and oxygen control. It has shown that the powders have good characteristics (spherical, smooth, flow well …) and it highly likely that further work will quickly optimise the size distributions to work better for L-PBF. The densities produced in the material were very encouraging and differences in mechanical strength and corrosion were probably more strongly related to the minor and controllable differences in composition, such as the higher Nitrogen content in the gas atomised powder, than to any major processing hurdles.

However, further work needs to be done. The identified differences need to be understood better, and the entire process optimised so that the goal of a rapid, combinatorial powder alloy development route can be achieved. One of the next steps will be a combinatorial study optimising properties around on one or more of the major alloying elements.

## Acknowledgements

The authors would like to thank LSN Diffusion for the gas atomised powder, and particularly Mitch and Ryan for undertaking the ICP and combustion analysis at such short notice. The authors would also like to thank Welding Alloys for providing the cored wire. The authors gratefully acknowledge the funding by the Welsh government to start the MACH1 laboratory and the COMET project, which has allowed us to do this work.

## References

[1] T. M. Pollock, A. J. Clarke, and S. S. Babu, "Design and Tailoring of Alloys for Additive Manufacturing," *Metall Mater Trans A Phys Metall Mater Sci*, vol. 51, no. 12, pp. 6000–6019, Dec. 2020, doi: 10.1007/s11661-020-06009-3.

[2] M. R. Stoudt, T. P. Battle, and D. L. Bourell, "Materials Research Needs for Development of Technical Standards in Additive Manufacturing," *JOM*, vol. 76, no. 4, pp. 1883–1884, Apr. 2024, doi: 10.1007/s11837-024-06400-0.

[3] R. Gradinger, "Herausforderungen bei der industriellen Umsetzung des Legierungskonzeptes Scalmalloy für Flugzeuganwendungen," *Berg Huettenmaenn Monatsh*, p. 440, Sep. 2009.

[4] K. Schmidtke, F. Palm, A. Hawkins, and C. Emmelmann, "Process and mechanical properties: Applicability of a scandium modified Al-alloy for laser additive manufacturing," in *Physics Procedia*, Elsevier B.V., 2011, pp. 369–374. doi: 10.1016/j.phpro.2011.03.047.

[5] Z. Zhu *et al.*, "Recent progress on the additive manufacturing of aluminum alloys and aluminum matrix composites: Microstructure, properties, and applications," *International Journal of Machine Tools and Manufacture*, vol. 190. Elsevier Ltd, Aug. 01, 2023. doi: 10.1016/j.ijmachtools.2023.104047.

[6] D. Schimbäck *et al.*, "Alloy design strategy for microstructural-tailored scandium-modified aluminium alloys for additive manufacturing," *Scr Mater*, vol. 207, Jan. 2022, doi: 10.1016/j.scriptamat.2021.114277.

[7] M. H. Mosallanejad, B. Niroumand, A. Aversa, and A. Saboori, "In-situ alloying in laser-based additive manufacturing processes: A critical review," *Journal of Alloys and Compounds*, vol. 872. Elsevier Ltd, Aug. 15, 2021. doi: 10.1016/j.jallcom.2021.159567.

[8] S. L. Sing *et al.*, "Title: Emerging Metallic Systems for Additive Manufacturing: In-situ Alloying and Multi-metal Processing in Laser Powder Bed Fusion."

[9] M. Ritchie *et al.*, "In-situ Modification of a High Entropy Alloy With 2.4% Molybdenum Using LPBF, and its Effect on Microstructure and Corrosion Resistance," in *Annual International Solid Freeform Fabrication Symposium*, Austin, Texas, USA, 2022.

[10] J. Gao *et al.*, "Accelerated discovery of high-performance Al-Si-Mg-Sc casting alloys by integrating active learning with high-throughput CALPHAD calculations," *Sci Technol Adv Mater*, vol. 24, no. 1, 2023, doi: 10.1080/14686996.2023.2196242.

[11] B. Bałasz, M. Bielecki, W. Gulbiński, and Słoboda, “Comparison of ultrasonic and other atomization methods in metal powder production,” *Journal of Achievements in Materials and Manufacturing Engineering*, vol. 116, no. 1, pp. 11–24, Apr. 2023, doi: 10.5604/01.3001.0016.3393.

[12] A. Yankin *et al.*, “Comprehensive analysis of ultrasonically atomized 316L stainless steel powder using adjusted additive manufacturing suitability factor,” *Powder Technol*, vol. 444, Aug. 2024, doi: 10.1016/j.powtec.2024.120004.

[13] F. Hinrichs *et al.*, “Flexible powder production for additive manufacturing of refractory metal-based alloys,” *Metals (Basel)*, vol. 11, no. 11, Nov. 2021, doi: 10.3390/met11111723.

[14] A. Zavdoveev *et al.*, “Non-equimolar Cantor high entropy alloy fabrication using metal powder cored wire arc additive manufacturing,” *Additive Manufacturing Letters*, vol. 6, Jul. 2023, doi: 10.1016/j.addlet.2023.100124.

[15] J. A. Cherry, H. M. Davies, S. Mehmood, N. P. Lavery, S. G. R. Brown, and J. Sienz, “Investigation into the effect of process parameters on microstructural and physical properties of 316L stainless steel parts by selective laser melting,” *International Journal of Advanced Manufacturing Technology*, vol. 76, no. 5–8, pp. 869–879, 2015, doi: 10.1007/s00170-014-6297-2.

[16] N. P. Lavery *et al.*, “Effects of hot isostatic pressing on the elastic modulus and tensile properties of 316L parts made by powder bed laser fusion,” *Materials Science and Engineering: A*, vol. 693, pp. 186–213, 2017.

[17] R. Douglas, N. Barnard, N. Lavery, J. Sullivan, T. Jones, and R. Lancaster, “The effect of powder recycling on the mechanical performance of laser powder bed fused stainless steel 316L,” *Addit Manuf*, vol. 88, p. 104245, May 2024, doi: 10.1016/j.addma.2024.104245.

[18] K. Murray *et al.*, “The influence of powder ageing characteristics on 316l stainless steel processed by laser based powder bed fusion,” in *Proceedings Euro PM 2017: International Powder Metallurgy Congress and Exhibition*, 2017.

[19] N. P. Lavery *et al.*, “Effects of hot isostatic pressing on the elastic modulus and tensile properties of 316L parts made by powder bed laser fusion,” *Materials Science and Engineering: A*, vol. 693, pp. 186–213, 2017, doi: 10.1016/j.msea.2017.03.100.

[20] I. S. Grech, J. H. Sullivan, R. J. Lancaster, J. Plummer, and N. P. Lavery, “The optimisation of hot isostatic pressing treatments for enhanced mechanical and corrosion performance of stainless steel 316L produced by laser powder bed fusion,” *Addit Manuf*, vol. 58, 2022, doi: 10.1016/j.addma.2022.103072.

[21] J. Boes, A. Röttger, L. Becker, and W. Theisen, “Processing of gas-nitrided AISI 316L steel powder by laser powder bed fusion – Microstructure and properties,” *Addit Manuf*, vol. 30, Dec. 2019, doi: 10.1016/j.addma.2019.100836.

[22] Z. Sun, X. Tan, and S. B. Tor, “Effects of chamber oxygen concentration on microstructure and mechanical properties of stainless steel 316L parts by selective

laser melting," in *Proceedings of the International Conference on Progress in Additive Manufacturing*, Pro-AM, 2018, pp. 470–475. doi: 10.25341/D4CS38.

[23] J. P. Choi *et al.*, "Evaluation of powder layer density for the selective laser melting (SLM) process," *Mater Trans*, vol. 58, no. 2, pp. 294–297, 2017, doi: 10.2320/matertrans.M2016364.

[24] N. P. Lavery *et al.*, "Effects of hot isostatic pressing on the elastic modulus and tensile properties of 316L parts made by powder bed laser fusion," *Materials Science and Engineering: A*, vol. 693, pp. 186–213, 2017.

[25] I. S. Grech, J. H. Sullivan, R. J. Lancaster, J. Plummer, and N. P. Lavery, "The optimisation of hot isostatic pressing treatments for enhanced mechanical and corrosion performance of stainless steel 316L produced by laser powder bed fusion," *Addit Manuf*, vol. 58, p. 103072, 2022.

[26] A. J. Cooper, W. J. Brayshaw, and A. H. Sherry, "Tensile Fracture Behavior of 316L Austenitic Stainless Steel Manufactured by Hot Isostatic Pressing," *Metall Mater Trans A Phys Metall Mater Sci*, vol. 49, no. 5, pp. 1579–1591, May 2018, doi: 10.1007/s11661-018-4518-2.

[27] Y. Shi, B. Yang, and P. K. Liaw, "Corrosion-resistant high-entropy alloys: A review," *Metals (Basel)*, vol. 7, no. 2, Feb. 2017, doi: 10.3390/met7020043.

[28] Allen J. Bard, Larry. R. Faulkner, and Henry S. White, *Allen J. Bard, Larry. R. Faulkner, Henry S. White: Electrochemical Methods: Fundamentals and Applications, 3rd edition, Wiley*, vol. 48, no. 6. Springer Science and Business Media LLC, 2023. doi: 10.1007/s11243-023-00555-6.

[29] "Designation: G61 − 86 Standard Test Method for Conducting Cyclic Potentiodynamic Polarization Measurements for Localized Corrosion Susceptibility of Iron-, Nickel-, or Cobalt-Based Alloys 1." doi: 10.1520/G0061-86R18.

[30] "Standard Test Method for Conducting Potentiodynamic Polarization Resistance Measurements 1." doi: 10.1520/G0059-97R20.

[31] M. Ritchie *et al.*, "In-situ Modification of a High Entropy Alloy With 2.4% Molybdenum Using LPBF, and its Effect on Microstructure and Corrosion Resistance," in *2022 International Solid Freeform Fabrication Symposium*, 2022, pp. 373–382. doi: http://dx.doi.org/10.26153/tsw/44564.

[32] N. Haghdadi, M. Laleh, M. Moyle, and S. Primig, "Additive manufacturing of steels: a review of achievements and challenges," *Journal of Materials Science*, vol. 56, no. 1. Springer, pp. 64–107, Jan. 01, 2021. doi: 10.1007/s10853-020-05109-0.